Influence of the Metal Support—Catalyst Contact on the Performance of NiO-Based O_2 Evolution Electrocatalysts

Harol Moreno Fernández,* Esmaeil Adabifiroozjaei, Tan Manuel Marcello Nathanael, Di Wang, Vanessa Wollersen, Mohan Li, Olaf Lindemann, Christian Kübel, Leopoldo Molina-Luna, and Jan P. Hofmann*

ABSTRACT: The performance of NiO-based electrocatalysts for the oxygen evolution reaction (OER) is strongly influenced by the interface between the metal support (current collector) and the catalyst layer, which modulates electronic properties and electrochemical activity. This study systematically investigates the solid−solid interface behavior of NiO thin films prepared by reactive magnetron sputtering on Pt, Au, and Ni, followed by electrochemical characterization. Stepwise NiO deposition and X-ray photoelectron spectroscopy reveal distinct band alignment and electronic structure differences at the metal−catalyst interface. NiO on Pt forms a Schottky barrier that facilitates charge separation but increases electron transfer resistance, resulting in the lowest current densities. NiO on Au exhibits superior OER performance, attributed to forming an interfacial NiAu oxide that enhances electrochemically active site density and modifies the electronic structure at the solid−solid and solid−liquid interfaces. High-resolution TEM reveals that NiO grains on Au adopt a metastable hexagonal structure along the [10−10] zone axis, deviating from the typical cubic phase. The absence of (001) and (010) reflections in FFT patterns suggests disrupted lattice periodicity caused by point or planar defects. These structural distortions may stabilize the hexagonal phase under strain and limited surface diffusion during deposition. NiO on Ni exhibits the lowest interfacial resistance and the highest current density, but is limited by a low electrochemically active surface area and sluggish kinetics, as reflected in a higher overpotential. Electrochemical impedance spectroscopy and band alignment confirm that interfacial electronic and structural modifications have a critical influence on catalytic activity. These findings highlight the importance of substrate selection and interface engineering, including defect-mediated metastability, in optimizing NiO-based OER anodes for next-generation alkaline water electrolysis systems.

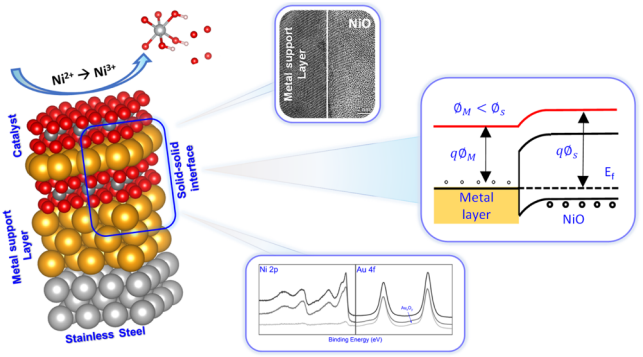

KEYWORDS: *oxygen evolution reaction, current collector, interface analysis, band alignment, XPS*

1. INTRODUCTION

Developing efficient and durable electrocatalysts for the oxygen evolution reaction (OER) is essential for advancing electrochemical energy conversion technologies. Nickel oxide (NiO) has garnered significant attention as a promising OER catalyst for alkaline water electrolysis (AWE) due to its abundance, stability, and favorable redox properties.[1,2] However, the underlying metal support layer, which also acts as a current collector, can significantly influence its electrochemical performance, as the interface between NiO and the metallic support plays a crucial role in modulating the electronic structure and charge transfer. Numerous studies have explored the impact of metal supports, such as Au, Pt, Cu, Ag, and Pd, on the catalytic activity of some transition metal oxides (TMOs).[3−9] Yeo and Bell demonstrated enhanced OER activity in Au-supported Ni and Co oxides, attributing this improvement to charge transfer from the transition metal to the electronegative Au substrate.[10,11] In their review, Liu et al.[12] collected available information on the mechanism of Au-driven OER, which follows the adsorption evolution mechanism (AEM) and the lattice oxygen-mediated mechanism (LOM). They showed that Au enhances the catalytic activity of most OER catalysts, a phenomenon attributed to the unique structural characteristics of Au and its interaction with other OER catalysts. Due to its high electronegativity, they also showed that Au incorporation into the oxidic catalyst enhances

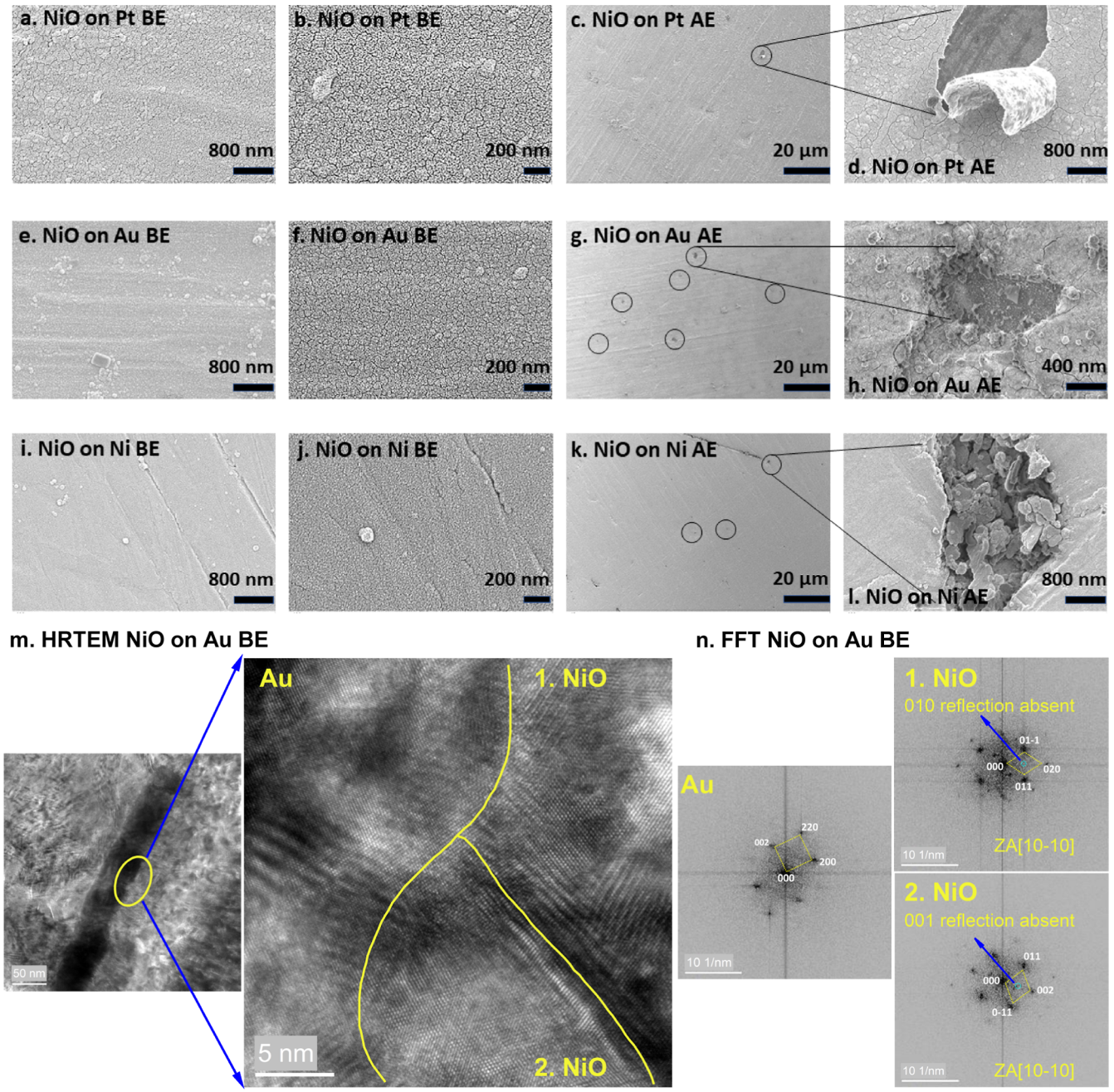

Figure 1. Physical characterization of NiO deposited on top of the three-metal support catalyst. (a,b) SEM images of NiO deposited on Pt before electrochemical conditioning (BE). (c,d) SEM images of NiO deposited on Pt after electrochemical conditioning (AE). (e,f) SEM images of NiO deposited on Au before electrochemical conditioning. (g,h) SEM images of NiO deposited on Au after electrochemical conditioning. (i,j) SEM images of NiO deposited on Ni before electrochemical conditioning. (k), (l) SEM images of NiO deposited on Ni after electrochemical conditioning. (m), HRTEM analysis at the Au−NiO interface before electrochemical treatment (n), FFT (Fast Fourier Transform) analysis providing a detailed crystallographic assessment of NiO deposited on gold (Au).

OER electrocatalysts through AEM and LOM mechanisms. In AEM, interfacial Au directly interacts with oxygen, accelerating the OER kinetics. In LOM, the enhancement of OER electrocatalysis arises from the synergistic interaction between incorporated Au and oxygen vacancies.[13,14] Such catalyst−substrate interactions can modify the binding energy of reaction intermediates by altering the electronic structure of active sites or directly participating in the reaction. Despite some existing literature reports exploring NiO in conjunction with platinum (Pt), gold (Au), or nickel (Ni) interactions[15−20] relevant to oxygen or hydrogen evolution reactions (OER/HER), a comprehensive understanding of solid−solid interactions in thin films and their relevance for the OER remains limited, necessitating further investigation into electrode-substrate interactions to accurately evaluate the intrinsic activity of OER catalysts.

In this study, NiO thin films were prepared on Pt, Au, and Ni substrates via reactive magnetron sputtering, ensuring precise control over film stoichiometry and surface morphology. Given the intrinsic structural and electronic property differences between metals and oxides, the interface plays a crucial role in determining electrochemical performance.

Metals exhibit atomic bonding primarily governed by interactions between metal ions and free electrons, resulting in a simpler and more ordered crystal structure with a higher coordination number. In contrast, oxides rely on ionic interactions between positive and negative ions, leading to more complex atomic arrangements. These fundamental differences contribute to variations in interfacial bonding, often resulting in weak mechanical adhesion and interfacial defects that impact electronic interactions, charge transfer, and catalytic activity.[21] X-ray photoelectron spectroscopy (XPS) and electrochemical characterization techniques were employed to investigate band-bending effects, electronic interactions, and the influence of substrate material on OER activity.

The primary goal is to determine how different supported metals between the current collector (in our case, polished stainless steel (SS)) and the catalyst (in our case, NiO) affect the catalytic performance of NiO in the OER. Charge transfer, interfacial chemistry, as well as electronic structure at this interface, influence the efficiency of the electrochemical processes occurring in the active catalyst layer, viz., capacitive charging/discharging, Faradaic processes like the activation of the catalyst ($NiO \rightarrow Ni(OH)_2 \rightarrow NiOOH$), and the OER itself. The study reveals that NiO deposited on Pt forms a typical Schottky barrier,[22] increasing the electron transfer resistance and thereby lowering the current density. In contrast, NiO on Au enhances OER performance due to the interfacial NiAu oxide, which increases active sites and modifies the electronic structure. NiO on Ni shows the lowest interfacial resistance and higher current density than NiO on Pt, but it suffers from poor reaction kinetics, as seen in its highest overpotential. The structural and mechanical disparities at metal/oxide interfaces thus influence interfacial charge transport and overall catalytic performance.

By correlating interfacial chemistry with electrochemical performance, this work provides fundamental insights into the role of metallic support layers in optimizing NiO catalysts, contributing to the rational design of high-performance OER electrodes. Understanding these interfacial effects is crucial for optimizing NiO-based catalysts and electrodes, thereby enhancing overall electrolyzer efficiency.

The manuscript is organized as follows. Section 2.1 presents the structural and chemical characterization of NiO thin films at their interface with Au, Pt, and Ni substrates, prior to any electrochemical testing, highlighting interfacial strain and defect formation. Section 2.2 examines the electronic structure using valence band XPS and UPS, with an emphasis on the role of defect states and band alignment. Section 2.3 correlates these findings with electrochemical OER performance based on cyclic voltammetry, changes in electrochemical active surface area, and impedance spectroscopy. The Methods section compiles all experimental procedures. The manuscript concludes with a discussion of the broader implications for interface and defect engineering in Ni-based electrocatalysts.

2. RESULTS AND DISCUSSION

2.1. Preparation and Physical Characterization of NiO Deposited on Pt, Au, and Ni Metal Support Layers. NiO thin films were deposited via reactive magnetron sputtering using 5% oxygen content in the plasma discharge. Under these conditions, the resulting film stoichiometry was $NiO_{1.01}$, close to the desired 1:1 Ni-to-O ratio. The deposition was made onto polished stainless steel (SS) foils coated with 50 nm of Pt, Au, or Ni. Previously used in our studies,[23−25] this technique enables the preparation of clean catalysts while controlling oxygen content and film thickness, key parameters for interface engineering and analysis. Deposition and analysis were conducted exclusively in an integrated ultrahigh vacuum (UHV) cluster tool, which comprises a deposition chamber and X-ray photoelectron spectroscopy (XPS) capabilities. This setup ensures process cleanliness and preserves the integrity of the thin film throughout.

The procedure involved sequential NiO depositions, beginning with 3 s and increasing incrementally to 8, 17, 34, 60, 120, and 1800 s. Each deposition was followed by an XPS analysis of core-level spectra and valence band (VB) to monitor changes occurring at the developing interface. Final NiO films, approximately 60 nm thick, were further characterized by scanning electron microscopy (SEM) before and after electrochemical testing. High-resolution transmission electron microscopy (HRTEM) was also used to characterize the NiO film deposited on Au. NiO prepared with 1% and 20% oxygen concentration in the plasma discharge deposited on Ni were also examined by (S)TEM, STEM−EDX, and STM-EELS spectrum imaging on cross-sectional specimens prepared by focused ion beam (FIB).

Figure 1a−l shows the SEM surface images revealing the nanostructure morphology of the thin films. Before electrochemical conditioning (BE) (Figure 1a,b,e,f,i,j), the NiO appears homogeneously distributed with irregular flat grains and no cracks or pinholes when deposited on the three metals. From Figure 1b,f,j, larger grain sizes are observed for NiO deposited on Pt, followed by Au, while the smallest grain sizes occur on Ni. Pinholes appear on the catalyst after electrochemical conditioning (AE) (Figure 1c,g,k).

A closer inspection of the thin films after the electrochemical conditioning (AE) was performed in the areas of interest (Figure 1d,h,l) to determine the nature of these holes. NiO deposited on Pt exhibits small delamination, which is not uniformly distributed across the film, exposing the metallic support layer (Figure 1d). In contrast, NiO on Au presents a higher number of holes across the sample, and a closer inspection (Figure 1h) reveals the absence of NiO in these regions, suggesting poorer adhesion to the Au support layer. Finally, for NiO on Ni (Figure 1l), NiO still covers the internal areas of the holes. However, it could be the Ni metallic sublayer being reoxidized during or after the electrochemical conditioning.

The oxygen content is a critical parameter to control, as its concentration in the plasma discharge during the thin film process influences the formation of defects, such as oxygen interstitials and nickel vacancies, which affect grain size and surface roughness.[26,27] Controlling these factors is essential to properly compare the effects of different metal support layers without being biased by significant variations in surface roughness or defect formations that could impact the OER performance.[23,28−30] To verify the impact of the metallic support layer on roughness, we analyzed NiO thin films deposited on Pt, Au, and Ni, employing 1% oxygen in the plasma discharge. As shown in Figure S1, under lower but identical oxygen partial pressure conditions, NiO exhibited a triangular pyramid-like structure[31] with the largest grain sizes observed for NiO on Pt, followed by Au, and the smallest for Ni. Additionally, Table S1 shows that NiO thin films on Pt exhibit the highest active surface area, followed by Ni, while the lowest is observed for Au. These significant differences in

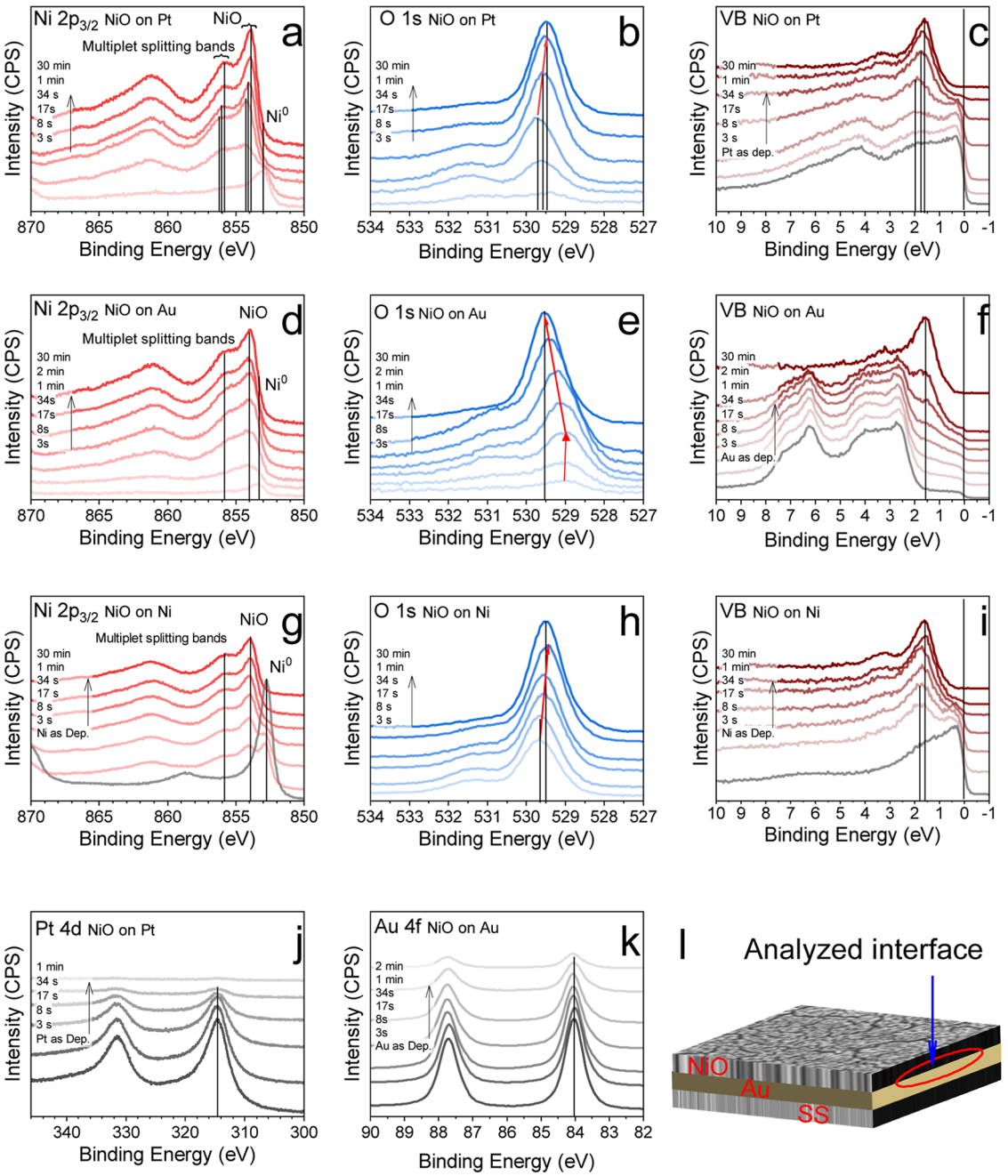

Figure 2. Interface analysis of NiO in a consecutive deposition step on different metals before any electrochemical conditioning. The estimated values are given in Table S2; therefore, 3 s corresponds to a ∼0.2 nm, 8 s to a ∼0.7 nm, 17 s to a ∼1.7 nm, 34 s to a ∼3.7 nm, 1 min to a ∼8 nm, and 30 min to a ∼60 nm. (a–c) Evolution of the Ni $2p_{3/2}$, O 1s, and VB in NiO deposited on Pt. (d–f) Evolution of the Ni $2p_{3/2}$, O 1s, and VB in NiO deposited on Au. (g–i) Evolution of the Ni $2p_{3/2}$, O 1s, and VB in NiO deposited on Ni. (j,k) Evolution of the Pt 4d and Au 4f, in the corresponding NiO depositions on these metals. (l) Schematic diagram showing the different layers and the interface being studied. All time labels (e.g., 3 s, 8 s, etc.) are shown in black and grouped for clarity; they indicate the sequential NiO deposition steps and correspond to the evolution of the spectra, but are not linked to specific curves to avoid overcrowding the plot.

roughness cannot be ignored when comparing the OER performance of these three systems.

Furthermore, we prepared NiO thin films on polished, mirror-like Ni foils with oxygen contents of 1%, 10%, and 20% in the plasma discharge. Figure S2 demonstrates that increased oxygen content reduces surface roughness, as reported by different authors.[27,32] This reduction in roughness correlates with a decrease in the redox wave amplitude, indicating a lower active surface area. However, despite the reduced active surface area, the OER activity improves with higher oxygen content (Figure S2d). These findings highlight the need to carefully consider surface roughness and oxygen content when comparing the OER performance of NiO thin films deposited on different metal–supported layers.

Additionally, Figure S2f,g displays the HRTEM and HRSTEM images of NiO thin films deposited on Ni metal by reactive magnetron sputtering using 1% and 20% oxygen content, respectively. The images reveal regions with distinct periodic lattice contrast for Ni and NiO. The oxide layer exhibits variations in lattice ordering and interplanar spacing

that are visually consistent with the characteristics of NiO. These differences become more pronounced with increasing oxygen content, indicating a thicker and more developed oxide layer at 20% oxygen. Figure S2h, i further supports this through EELS elemental mapping, where the distribution of oxygen (O K-edge) is localized to the oxide layer and is more intense in the 20% sample, suggesting more extensive oxidation. The Ni $L_{2,3}$ and O K signals align spatially with the observed structural features, confirming the coexistence of Ni and an oxygen-rich phase at the surface.

Figure 1m, n presents an HRTEM analysis of the NiO−Au interface, along with the corresponding fast Fourier transform (FFT), respectively. The HRTEM image (Figure 1m) shows a well-defined interface between crystalline Au and two distinct NiO grains, marked by a yellow grain boundary. FFT patterns (Figure 1n) from each region reveal a face-centered cubic (fcc) structure for Au along the [001] zone axis, as evidenced by strong 002, 220, and 200 reflections. However, both NiO grains exhibit diffraction patterns consistent with a hexagonal structure along the [10−10] zone axis, which differs from the typical cubic NaCl-type structure of bulk NiO.[32,33] The absence of reflections such as (001) and (010) in the FFT patterns of NiO indicates a loss of periodicity along the *c*- and *a*-axes of the hexagonal lattice, pointing to the presence of point or planar defects within key crystallographic planes. These structural defects disrupt lattice order and could play a role in stabilizing metastable polymorphs, as studied in another system by Solomon et al.[34] Recent research has introduced the concept of metastable defect phase diagrams (MDPD), which incorporate the effects of defects into phase stability predictions, demonstrating that defect structures can stabilize phases not observed under equilibrium conditions.[35−37]

These observations suggest that the growth of NiO on Au under oxygen partial pressure and at room temperature may favor or stabilize a noncubic phase due to substrate-induced strain or limited surface diffusion during deposition.

The structural disorder observed in the hexagonal NiO grains may also influence the material's electronic and catalytic behavior. Planar and point defects are known to introduce localized states within the band gap, which can alter the local density of states and facilitate charge transfer at the interface. Such effects are particularly relevant for electrocatalysis, as they may promote enhanced conductivity and the activation of surface oxygen species as presented by Qianyun et al. in their comprehensive review on defect-modulated electrocatalysis.[29] Although the active phase during OER is generally NiOOH, the structure and defect environment of the precursor NiO layer can affect the formation and properties of the oxidized phase. In particular, a hexagonal, defect-rich NiO may yield a more disordered or reactive NiOOH, potentially improving redox activity and contributing to the enhanced OER performance observed for NiO on Au. The catalytic performance of these thin films is examined in detail in Section 2.3, where it is correlated with electrochemical measurements.

While surface characteristics are important for OER, these findings show that the buried catalyst-metal interface also plays a critical role by influencing defect formation, electronic structure, and ultimately, electrocatalytic behavior.

2.2. Interface Analysis of the Solid−Solid Contact (Metal Support Layer-Catalyst). To investigate the electronic and chemical nature of the NiO−metal interfaces, we monitored the evolution of the Ni 2p, O 1s, Pt 4d, and Au 4f core levels and valence band spectra during sequential NiO deposition at 8, 17, 34, 60, 120, and 1800 s. These XPS features provide information about energy level alignment (via binding energy shifts), oxidation state changes (via multiplet splitting and peak shape), and chemical interactions (such as interfacial oxide formation). In the following discussion, we interpret spectral changes by distinguishing between electronic effects, such as band bending, and chemical effects, including oxidation or possible alloying. The data are presented and analyzed in the order of Pt → Au → Ni for consistency with the experimental sequence and to aid comparison across systems.

The corresponding XPS analysis of the Ni $2p_{3/2}$ spectra for the deposited NiO on Pt and Au (Figure 2a,d) at very low thicknesses (∼0.2 nm, corresponding to 3 s of deposition) show a shift at the near-interface, locating the Ni $2p_{3/2}$ at 853.2 eV, which is 0.8 eV lower than the NiO nominal position. This shift suggests that a fully evolved NiO band structure is not present at very low thicknesses (∼0.2 nm), which is below the cubic NiO lattice constant (0.43 nm)[38] or the hexagonal NiO lattice (a = 0.29 nm, c = 0.34 nm).[39] Therefore, the initial observed binding energy shift is attributed to interface-induced electronic effects, such as Fermi level alignment and charge redistribution, as well as incomplete structural formation during the initial stages of film growth.

For NiO deposited on Pt, the Ni $2p_{3/2}$ spectrum at the 8 s deposition step shows a well-resolved multiplet splitting band at 856 eV (Figure 2a), characteristic of Ni^{2+} in NiO and indicating no apparent formation of a Ni−Pt alloy at the interface. This conclusion is further supported by the agreement between the overlayer thickness calculated using the Lambert−Beer law[41] from the XPS interface experiment and the thickness estimated from profilometry calibrations (Table S2). If significant alloying or interdiffusion had occurred at the interface in this sample, the actual film thickness measured by XPS attenuation would deviate from the expected values due to the formation of a mixed interfacial layer or buried species not accounted for by a pure NiO overlayer model. The observed consistency between the calculated XPS interface and the estimated profilometer thicknesses thus suggests that there is no chemical reactivity between Ni and Pt.

In addition, as the NiO film grows, the Ni $2p_{3/2}$ peak, initially at 854.2 eV at 8 s, shifts to 853.9 eV for the 60 s deposition step. A similar shift is observed in the O 1s peak (from 529.8 to 529.4 eV) and in the valence band maximum (VBM) (Figure 2b,c) shifts, which we attribute to the band bending of NiO at the platinum interface.

For NiO deposited on Au (Figure 2d−f), it is not easy to clearly distinguish between electronic and chemical shifts; this is due to the significant spectral changes observed in the Ni 2p region (Figure 2d), especially during the first five deposition steps (3, 8, 17, 34, 60 s). The Ni 2p multiplet splitting bands are poorly resolved for NiO deposited on Au, in contrast to the well-defined features at 856.0 eV observed for NiO deposited on Pt. Similarly, the O 1s peak shifts differently for NiO on Au (from 529.0 to 529.4 eV) compared to NiO on Pt, further complicating the interpretation.

To further explore the NiO−Au interface, we conducted an additional deposition experiment using increased oxygen content (Figure S3); this revealed clear evidence of Au_xO_y formation during the first 59 s (corresponding to the third deposition step, ∼6 nm NiO). The observed shift in the O 1s peak at this stage is likely associated with Au-oxidation.

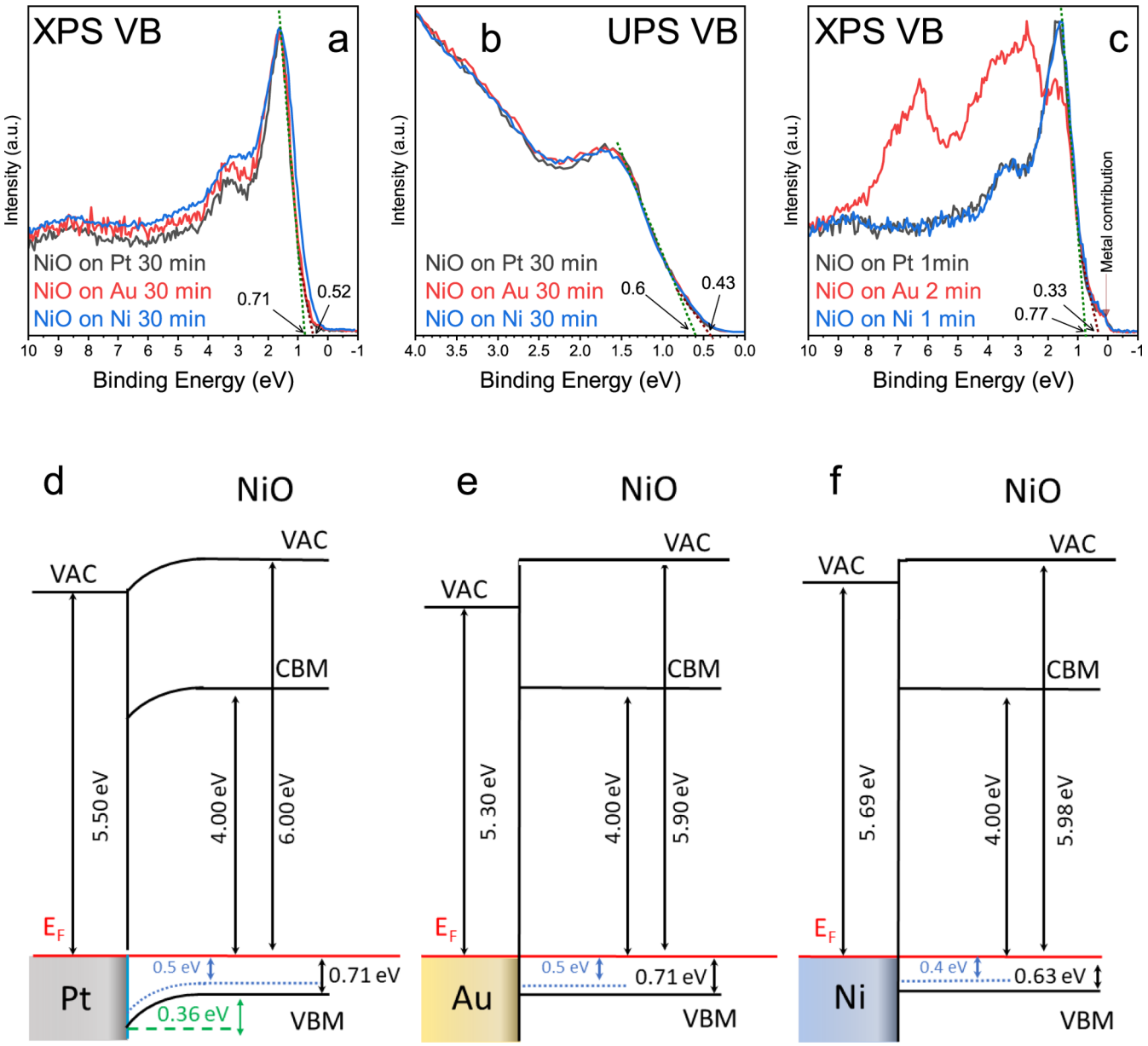

Figure 3. XPS and UPS Valence band and interfacial band alignment diagrams. (a) Valence band as measured with XPS, with the corresponding VBM for the ~60 nm NiO deposited on Pt, Au, and Ni. (b) Valence band as measured with UPS, with the corresponding VBM for the ~60 nm NiO deposited on Pt, Au, and Ni. (c) Valence band as measured with XPS, with the corresponding VBM for the ~8 nm NiO, corresponding to the 1 min NiO deposition step on Pt, and Ni and 2 min NiO on Au. Figure (d–f) show the calculated work function for the final ~60 nm NiO layer deposited on different metals and the calculated work function of Pt, Au, and Ni as deposited on SS in UHV. (d) The band diagram for NiO on Pt shows a clear bending of NiO at the interface. (e) The band diagram for NiO on Au shows a flat band. (f) The band diagram for NiO on Ni shows a flat band. The blue dotted lines represent the tails measured at the valence band.

Meanwhile, the Ni 2p spectra continue to show poorly resolved multiplet splitting bands, even after 60 s of deposition (Figure S3a), suggesting the formation of a mixed NiAu oxide at the interface. This behavior aligns with previous reports of alloy-like NiAu oxide structures in thin films with 1.1 monolayers of NiO or nanoparticle sizes of 2 nm.[10,40]

On the other hand, for NiO deposited on nickel, the O 1s and VB shifts (Figure 2h,i) cannot conclusively indicate band bending at the interface. These changes could instead result from oxidation of the nickel metal support sublayer, where Ni transitions from Ni^0 to Ni^{2+} upon exposure to oxygen during the deposition process or by reacting with deposited NiO. This distinction emphasizes the challenges of interfacial analysis for NiO deposited on nickel, particularly when compared to platinum.

For the final NiO layer at 1800 s, the O 1s spectra for the three systems (Figure 2b,e,h) exhibit a main peak at 529.4 eV, attributed to the lattice oxygen atoms in NiO and an additional shoulder between 531.0 and 531.5 eV, which is associated with structural disorder in the film, as previously reported in literature.[42,43]

Furthermore, the detection of Au in the NiO film after 120 s of deposition for samples before any electrochecmial treatment (>10 nm thickness, Figures 2k and S3a) could indicate some metallic interdiffusion of Au into the NiO layer, a phenomenon previously observed in $NiCeO_x$-Au coatings by Desmond et

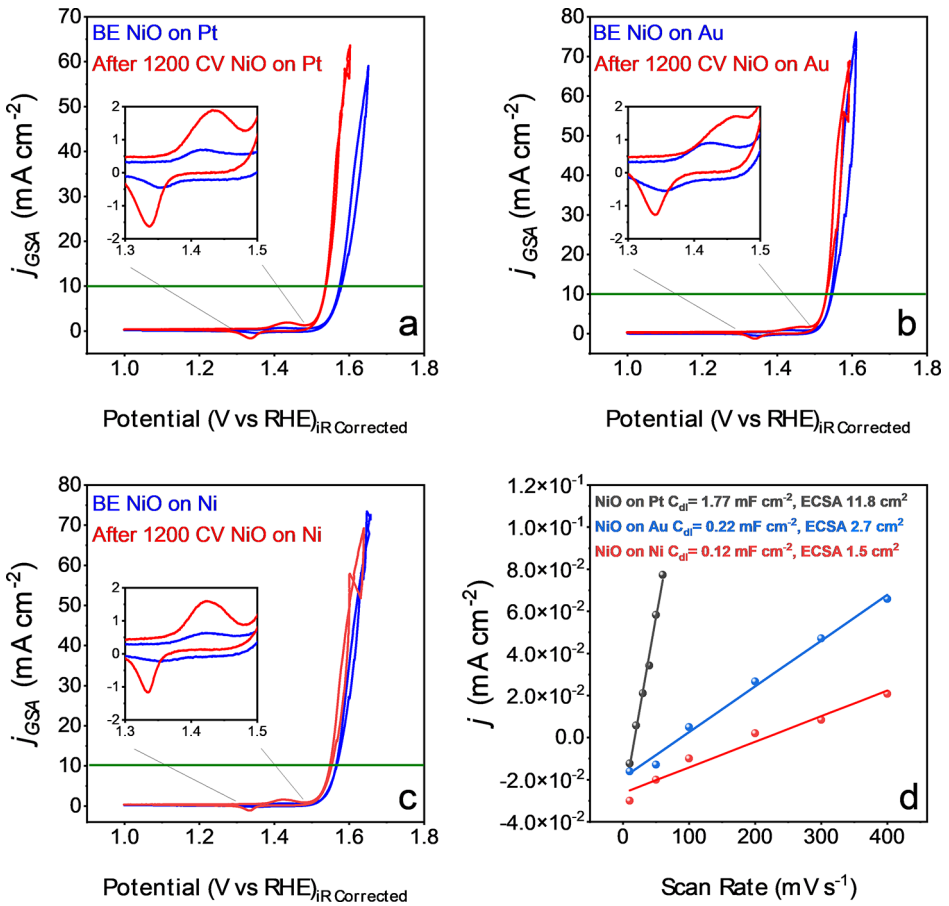

Figure 4. Cyclic voltammograms and ECSA. The current density is normalized to the geometric surface area (GSA) of the electrode. (a–c) Cyclic voltammograms of NiO deposited on Pt, Au, and Ni, respectively, before the 1200 cycles conditioning (blue lines) and after 1200 cycles conditioning from 1.0–1.5 V (vs RHE) at 100 mV s^{-1} (red lines). (d) ECSA values calculated from cyclic voltammograms for NiO deposited on Pt, Au, and Ni before 1200 cycles electrochemical conditioning. Note: BE = before electrochemical conditioning; AE = after electrochemical conditioning.

al.;[8] however, this observation was not visible in the STEM-EDS analysis of the FIB cross-section (Figure S4) probably due to the uneven surface of the specimen.

Interdiffusion between different materials has been widely studied[21,44−47] and it is partially influenced by the film structure, where defects such as dislocations, vacancies, and grain boundaries serve as diffusion pathways for atomic species. These defects facilitate mass transport across film interfaces, significantly impacting overall diffusivity. Grain boundaries rapidly accumulate foreign material, enabling interdiffusion at the interface, along the grain boundaries, and into adjacent lattices. However, the extent of interdiffusion is also dictated by lattice mismatch, which plays a crucial role in determining interfacial stability. For instance, the formation of AuNi oxide, but not PtNi oxide (Figure 2a,d), can be attributed to the lattice mismatches. Considering their respective lattice constants, 4.170 Å for NiO, 3.923 Å for Pt, and 4.078 Å for Au;[38,48,49] while the mismatch between Au and NiO is relatively low (2.2%), the mismatch between Pt and NiO is much higher (6.3%), leading to increased interfacial strain, which the system mitigates by forming dislocations that act as diffusion barriers, reducing atomic intermixing.

Beyond structural considerations, the reactivity of the metal-oxide interface significantly influences interdiffusion behavior.[21,50] In our case, NiO on Pt represents a nonreactive interface, where charge redistribution occurs without significant bond breaking, resulting in negligible interdiffusion, which explains why we do not observe the formation of a new oxide phase at the NiO−Pt interface. On the other hand, NiO on Au exhibits a more reactive interface, where charge transfer leads to the breaking of existing bonds and the formation of new chemical states. This reactivity may promote the formation of interfacial Au−NiO bonding environments or localized chemical states, such as partially oxidized Au or non-stoichiometric NiO, which modify the electronic structure at the interface, as suggested by the observed spectroscopic shifts and structural disorder.

At the atomic level, lattice mismatch-induced strain is often accommodated through reconstruction of the interfacial atomic arrangement, where atoms shift from their regular lattice positions to minimize strain energy. This structural disorder, caused by vacancies, dislocations, and interfacial strain, affects the local density of states (DOS), resulting in variations in interfacial bonding strength. A higher DOS at the Fermi level strengthens interfacial bonding, influencing charge redistribution at the interface, as shown by Lobzenko et al.[51]

To explore this experimentally, we analyzed the valence band region of NiO films using XPS and UPS to identify signatures of such defect-induced states. XPS and UPS valence band measurements (Figure 3a–c) for both thick (~60 nm) and thin (~8 nm) NiO films provide insight into the occupied electronic states near the Fermi level for samples deposited on

Pt, Au, and Ni. XPS (for samples of 60 nm thickness), with a probing depth of ∼5−8 nm, identifies a VBM at 0.71 eV for NiO on Pt and Au, and 0.63 eV for NiO on Ni, with a defect-induced tail extending to ∼0.5 eV below the Fermi level. These defects perturb the band edges by inducing potential deformation effects and creating impurity state bands.[23,52] UPS, with higher surface sensitivity (∼1−2 nm), reveals similar valence band tailing down to ∼0.43 eV (Figure 3b), confirming that these states are also present at the surface.

Furthermore, valence band tailing is already evident at the early deposition stage at 1 min step process (which correspond to a total of 2 min NiO deposition, aprox. ∼8.0 nm NiO layer, Figure 3c), showing a VBM for NiO at 0.77 with a band tail extending to 0.43 eV below the Fermi Level, indicating that defect-related states form from the onset of NiO growth and are not limited to thicker films, supporting the interpretation that defects originate near the metal-oxide interface and persist throughout the film. The consistent presence of tailing in both UPS (surface-sensitive) and XPS (subsurface-sensitive) spectra confirms that these states span several nanometers into the film, rather than being confined to the surface, underlining the substantial impact of early stage structural disorder on the electronic structure of the catalyst layer.

The corresponding NiO work functions, measured with XPS for the final layer deposited at 1800 s on Pt, Au, and Ni, are 6.00, 5.90, and 5.98 eV, respectively. Table S3 shows the corresponding work functions as measured by XPS. Although the work function involves bulk electronic properties,[53,54] it is fundamentally a surface-sensitive quantity that depends strongly on surface atomic structure, reconstruction, crystallographic orientation, and the presence of adsorbates or impurities.[55] The work function is crucial in governing the efficiency of interface electron transfer, a key factor in electrocatalysis. Differences in the work function between materials substantially influence band alignment and carrier transport, important factors in catalytic performance.[30,56−60]

Since band bending depends on the relative work functions of the metal and NiO, a larger work function mismatch results in stronger band bending, potentially forming Schottky barriers, while a smaller mismatch leads to an ohmic contact. In NiO deposited on Pt (with a work function difference of 0.5 eV), a Schottky-type band structure, presented in Figure 3d, was extracted from the interface XPS evolution of the Ni 2p core levels, suggesting a depletion layer at the interface, which could influence charge transfer kinetics by limiting electron transport. In contrast, for NiO deposited on Au, despite the largest work function difference of 0.6 eV between the Au and NiO, the formation of NiAu oxide may disrupt the NiO electronic structure, preventing the expected band bending. Our results reveal that NiO deposited on Ni exhibited the smallest work function difference (0.25 eV) between the metal and NiO. Although small shifts are observed in the O 1s and valence band spectra (Figure 2h,i), no visible Ni 2p level shifts are detected, indicating minimal or nonexistent band bending; therefore, the system can be assigned a flat-band configuration (Figure 3f). The lack of a significant interface potential barrier indicates that NiO−Ni interactions are likely governed by chemical bonding or interfacial oxidation rather than electrostatic band realignment. Such a configuration may facilitate electron exchange at the interface, which is relevant for catalytic applications where efficient charge transfer is necessary.

2.3. Electrochemical Evaluation. Having established the electronic structure of NiO deposited on different current collectors, we now evaluate the electrochemical performance of NiO thin films on Au, Pt, and Ni substrates. The electrochemical testing of NiO thin films was conducted in unpurified 1 M KOH using a three-electrode electrochemical cell, as described in previous papers.[23,24] The cyclic voltammogram measured before conditioning the samples (Figure 4a−c) showed that NiO on Au achieved the highest current density (reported with respect to the geometric surface area) of 76.1 mA cm^{-2} at 380 mV overpotential, followed by NiO on Ni with 72.7 mA cm^{-2} at 420 mV overpotential, and the lowest for NiO deposited on Pt with 59.1 mA cm^{-2} at 420 mV overpotential. However, the overpotentials required to reach 10 mA cm^{-2} were significantly higher than some literature values,[8,61,62] with 310 mV for NiO on Au and 340 mV for NiO on both Pt and Ni. After the electrochemical conditioning consisting of 1200 cyclic voltammograms from 1.0−1.5 V (vs RHE) at 100 mV s^{-1} scan rate, the overpotentials required to reach 10 mA cm^{-2} decreased to 300 mV, 310 mV, and 320 mV for NiO deposited on Au, Pt, and Ni, respectively. Interestingly, despite NiO on Pt exhibiting the highest electrochemical surface area (ECSA) and the most pronounced redox wave amplitudes (Figure 4d), it showed the lowest current density. Conversely, NiO on Ni, despite having the lowest ECSA values and the highest overpotential, demonstrates a better current density maximum than NiO on Pt. The superior performance of NiO on Au, achieving the lowest overpotential and highest oxygen evolution reaction (OER) activity, suggests a significant catalyst−substrate interaction due to the formation of AuNi oxides at the interface.[8,10,63] As mentioned by Strickler et al.,[64] the overpotential and enhancement when having an Au support film is not likely a result of increased conductivity, which we can corroborate with the electrochemical impedance spectroscopy (EIS) results, where the resistance for NiO on Au is considerably higher than NiO deposited on Ni or Pt. They attribute the enhancement to Au-facilitated Ni-oxidation or the formation of an AuNi interfacial oxide. However, for this to happen in our system, the KOH would need to interact with the metal layer near the metal-catalyst interface and not only at the catalyst−liquid interface following the lattice oxygen-mediated mechanism (LOM), as the catalyst constantly undergoes dynamic changes, oxidation, exchange, and release of oxygen ligands at the surface during the OER. If the reaction process happened near the Au−NiO interface (however, not necessarily in contact with the Au), Au would enhance the activity of oxygen vacancies and promote the direct formation of O−O bonds by the LOM mechanism, thus providing high OER activity, as studied by Chao and Liu et al.[12,13] To verify this assumption, we analyze the XPS measurement, which reveals a tenue Au signal in the Au 4f region (Figure S5). Additionally, SEM Figure 1g,h exposed small pinhole areas for NiO deposited on Au, which may indicate that at some point in the electrochemical reaction, KOH could have interacted with the metal−supported layer.

Taken together, these observations suggest that the NiO−Au interaction is not only structurally present but may also directly influence the catalytic mechanism. The Au−NiO mixture at the interface could modify the electronic structure by enhancing the hybridization between Ni 3d and O 2p orbitals, which facilitates oxygen vacancy formation and stabilizes high-valent Ni species, both of which are critical

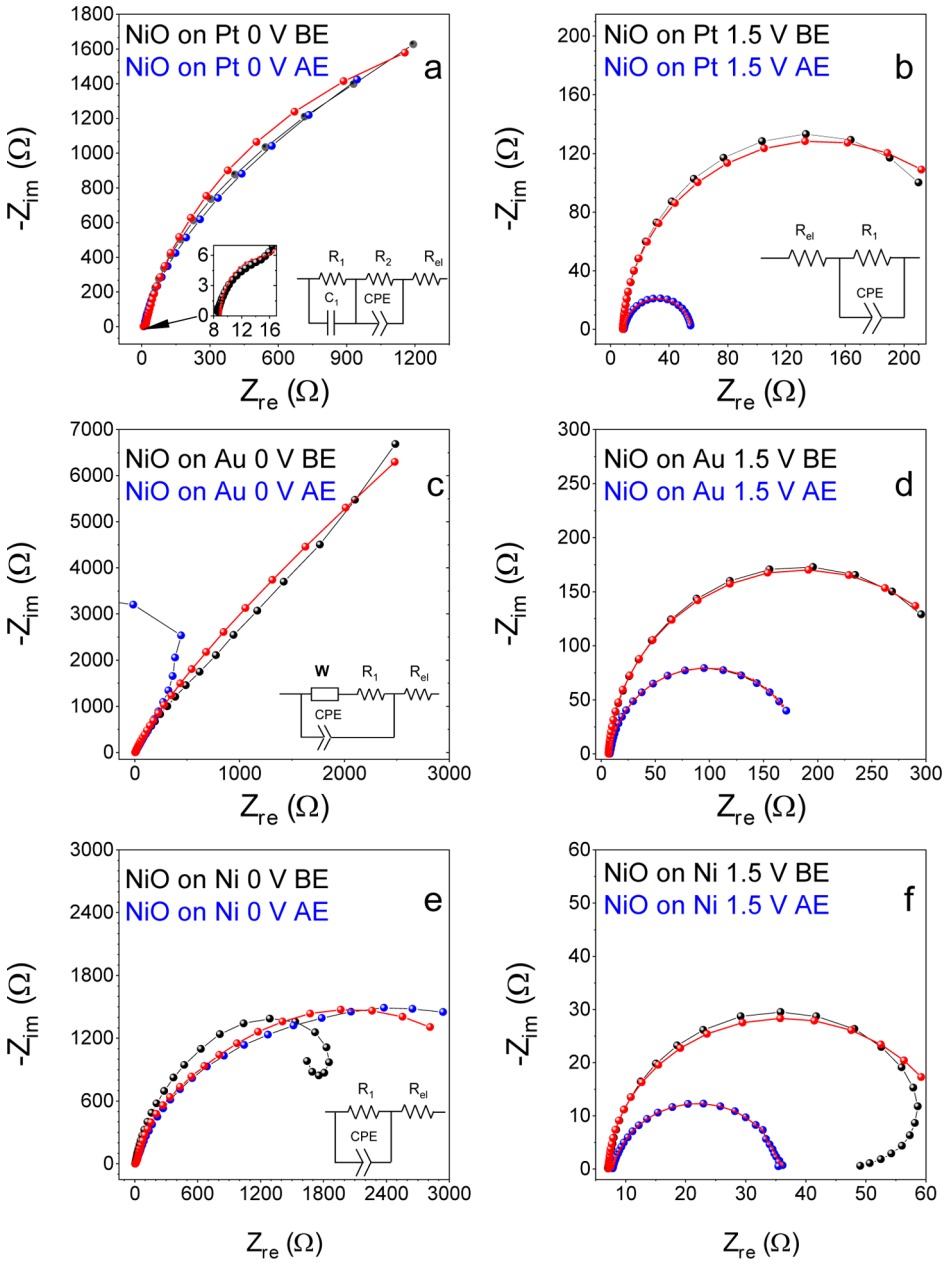

Figure 5. Nyquist representations of electrochemical impedance spectroscopy (EIS) data. (a,b) NiO on Pt before and after electrochemical conditioning at 0.0 and 1.5 V (vs RHE) at 100 mV s^{-1}. (c,d) NiO on Au before and after conditioning at 0.0 and 1.5 V (vs RHE) at 100 mV s^{-1}. (e,f) NiO on Ni before and after electrochemical conditioning at 0.0 and 1.5 V (vs RHE) at 100 mV s^{-1}. The red lines correspond to the fitting. For NiO on Au and Ni in Figures (d) and (f), the equivalent circuit is the same as in NiO on Pt, Figure (b). Note: BE = before electrochemical conditioning; AE = after electrochemical conditioning.

for activating the lattice oxygen-mediated mechanism (LOM). Several studies have shown that tuning the bulk electronic structure of transition metal oxides—particularly by raising the oxygen 2p-band center and increasing metal−oxygen covalency—can significantly promote OER activity.[65,66] Grimaud et al.[67] demonstrated that increased metal−oxygen covalency not only enhances OER kinetics but also enables the participation of lattice oxygen, thus opening up alternative reaction pathways beyond the classical surface metal-site mechanisms.

While our study does not directly probe LOM, the presence of pinholes (Figure 1g,h) and a detectable Au signal at the surface after electrochemical conditioning (Figure S5) suggests that the electrolyte may access the NiAu interface allowing the interfacial region to participate in lattice oxygen activation, consistent with previous studies by Liu et al.[12] and Chao et al.[13]

Figure 5 presents a series of electrochemical impedance spectra (EIS) recorded at 0.0 and 1.5 V DC offset (vs RHE) before and after electrochemical conditioning, displayed in the Nyquist (complex plane) representation. At 0.0 V, the surface is primarily composed of NiO or $Ni(OH)_2$, whereas at 1.5 V, the system operates in the Faradaic region where Ni^{2+} fully transforms into Ni^{3+} at the surface level.[24] As previously reported,[24,25] the electrochemical conditioning through 1200 CV cycles facilitates the transformation of the material into $Ni(OH)_2$. Upon applying 1.5 V, this phase oxidizes to Ni^{3+} (NiOOH), decreasing the charge transfer resistance (R_{ct})

across all three systems. The reduction in R_{ct}, along with an increase in the Q value of the constant phase element (CPE), indicates higher admittance and suggests an increased number of active sites on the electrode surface. However, as more $Ni(OH)_2$ forms, the dispersion parameter (α) decreases, indicating a shift away from ideal capacitive behavior (Table S4). This decrease in α reflects increased surface heterogeneity, suggesting that although the electrode surface becomes more electrochemically active, its nonuniformity compromises capacitive performance.

At 1.5 V DC offset, the impedance response of NiO deposited on Au (Figure 5d) shows a characteristic semicircle that closely matches that of NiO on Pt, suggesting similar charge transfer characteristics. However, the significantly higher R_{ct} of NiO on Au than NiO on Pt or Ni indicates that its superior OER performance is not driven by enhanced conductivity, confirming previous studies.[64] In contrast, NiO on Ni (Figure 5f) exhibits the lowest R_{ct}, measured at just 35 Ω, indicating superior charge transfer efficiency. This substantial reduction in charge transfer resistance is likely due to the favorable band alignment between NiO and Ni (Figure 3f), which minimizes interfacial resistance and enhances charge mobility. This enhanced charge transfer efficiency contributes to superior electrochemical performance compared to NiO on Pt.

Figure 5e,f also displays an inductive loop in the low-frequency region for the nonconditioned sample at 0.0 and 1.5 V (vs RHE). The inductive loop likely arises from the adsorption and desorption of intermediates on the electrode surface.[68−70] However, this feature was not well represented in the fitting simulation; thus, the corresponding equivalent circuit models do not include it.

The Nyquist representation of NiO on Ni at 0.0 V DC (Figure 5e) can be modeled using an equivalent circuit model similar to that used for the system at 1.5 V DC. However, the resistance observed at 0.0 V DC is not associated with charge transfer resistance, as no Faradaic reactions occur at this potential due to the absence of redox activity. Instead, the progressive increase in resistance, reaching 2940 Ω after 1200 CV cycles, suggests an inhibited electrochemical interaction between the electrolyte and the electrode. This behavior is likely due to the intercalation of water molecules, which promotes the formation of α-$Ni(OH)_2$ on the electrode surface. The increased presence of α-$Ni(OH)_2$ results in higher resistance, which correlates with the reduced maximum current density observed after electrochemical conditioning (Figure 4c).

The Nyquist plot for NiO on Pt at 0.0 V DC (Figure 5a) shows similar impedance characteristics before and after electrochemical conditioning. However, a distinct small semicircular loop appears in the high-frequency region before conditioning. This well-defined small semicircle corresponds to the initial stage of the equivalent circuit model, characterized by low R_1 and C_1 values. This feature is likely linked to the electrode−electrolyte interface, as it appears adjacent to R_{el} in the Nyquist plot. The remainder of the equivalent circuit model follows a Randles circuit representation, describing the charge transfer and diffusion processes.

Before conditioning, the Nyquist response of NiO on Au (Figure 5c) is best represented by a constant phase element (CPE) to account for nonideal capacitive behavior. Since no charge transfer reactions occur, a Warburg element is introduced to describe diffusion-controlled processes. This Warburg impedance originates from diffusion-controlled processes related to water intercalation during the phase transition from NiO to α-$Ni(OH)_2$ rather than charge transfer across the electrode−electrolyte interface. After electrochemical conditioning, the Warburg element disappears, indicating the complete surface transformation of NiO into α-$Ni(OH)_2$ across the film.[24]

In addition, these three systems were compared to NiO deposited on clean SS and used as a reference system, where no metal support layer was added. Although the ECSA value of 8.6 cm^2 is considerably larger than the ECSA for NiO deposited on Au and Ni, consisting of 2.7 cm^2 and 1.6 cm^2, Figure S7a shows that the maximum current density before electrochemical conditioning of 50 mA cm^{-2} at 360 mV overpotential is the lowest compared to the three systems. After the 1200 conditioning cycles, the overpotential at 10 mA cm^{-2} is reduced from 360 mV to 330 mV, which is not better than the 300 mV, 310 mV, and 320 mV for NiO deposited on Au, Pt, and Ni, respectively. Finally, the electrochemical impedance spectroscopy (EIS) spectra recorded at 0.0 and 1.5 V DC offset (vs RHE) before and after electrochemical conditioning displayed in the Nyquist (complex plane) representation in Figure S7d shows increased resistances reaching 1000 Ω at 1.5 V DC and 6000 Ω at 0.0 V DC, indicating a high charge transfer resistance at the catalyst−substrate interface.

3. CONCLUSIONS

This work highlights the critical role of the metal support layer in modulating the electrocatalytic behavior of NiO thin films for the oxygen evolution reaction. Through comparative analysis of Pt, Au, and Ni support metals, we demonstrate that the interfacial electronic structure—governed by band alignment, charge transfer resistance, and surface chemistry—directly impacts the kinetic and thermodynamic aspects of OER activity.

NiO on Au emerged as the most catalytically active configuration, achieving the lowest overpotentials and highest current densities, likely due to the favorable formation of interfacial oxides and the activation of lattice oxygen pathways. Despite exhibiting a relatively high interfacial resistance, its performance appears to be driven by interfacial electronic effects such as defect-induced valence band states and band alignment shifts observed in XPS/UPS, along with likely charge redistribution at the metal−oxide interface, which facilitates catalytic turnover without necessarily improving overall conductivity. In contrast, NiO on Ni, while displaying the lowest charge transfer resistance and a favorable ohmic contact, was limited by slower reaction kinetics and higher overpotentials, reflecting a low intrinsic catalytic activity. NiO on Pt formed a Schottky-type barrier that hindered efficient electron transfer, suppressing catalytic activity despite good charge carrier separation.

These findings reveal that the metal support is not merely a passive current collector but an active component that influences interfacial energetics and catalytic pathways. Optimal performance arises not from minimizing resistance alone, but from achieving a synergistic balance between interfacial charge transfer, catalytic site accessibility, and favorable reaction energetics. These findings highlight the significance of substrate selection and interfacial electronic structure engineering in designing next-generation electrocatalyst systems.

While this study focused on single-interface systems, future investigations involving multilayer configurations, such as NiO deposited on thin Au layers precoated onto Ni or Pt substrates, could offer deeper insight into how buried metal layers influence the interfacial electronic structure and catalytic activity. These stacked systems may allow further tuning of charge redistribution, band alignment, or oxygen species activation, and represent a promising direction for continued exploration.

4. EXPERIMENTAL SECTION

4.1. Preparation of NiO Thin Films. Stainless steel (SS) foils of 1 cm^2 were polished using 15 and 8 μm silicon carbide (Starcke, Struers) and 0.5 μm alumina paste (MicroPolish Alumina, Buehler). After that, they were cleaned sequentially in an ultrasonic bath with acetone, isopropanol, and Millipore water for 10 min each. They were loaded into the deposition chamber, which is a UHV chamber containing a magnetron sputtering source from MeiVac (MAK 2″). The chamber is part of the DAISYFUN cluster tool (DArmstadt's Integrated SYstem for FUNdamental research), integrating thin film preparation and XPS surface analysis (Figure S9a). The NiO thin films were prepared at room temperature by DC magnetron sputtering using a Ni target (Kurt J. Lesker with purity 99.99%) in a system with a base pressure of 1.0×10^{-9} mbar. Two mass flow controllers (MKS) introduced 1.0 sccm of O_2 and 19.0 sccm of Ar (Air Liquide with purity 99.995% and 99.999%, respectively). The working pressure was set to 3×10^{-2} mbar, and the plasma power to 15 W, with a substrate-to-target distance of 20 cm.

4.2. Electrochemical Characterization. Electrochemical measurements were conducted in a three-electrode setup in a PECC-2 cell from Zahner Elektrik, controlled by a potentiostat from Gamry Instruments (Interface 1000E) (Figure S9b). All measurements were performed in 1 M KOH (Carl Roth, unpurified, Fe < 7 ppb by ICP-OES). The same KOH solution was used consistently across all measurements, including NiO on Au, Pt, Ni, and stainless steel (SS), to ensure valid internal comparisons despite the presence of trace impurities.

Before the measurement, a Hg/HgO reference electrode from ProSense was calibrated against a reversible hydrogen electrode (RHE) (HydroFlex, Gaskatel). The counter electrode was a platinum wire. By an electrochemical impedance measurement at OCP, the current response during cyclic voltammetry (CV) was manually iR-corrected in the data post-treatment. The conditioning consisted of 1200 voltammetry cycles in the 1.0 V - 1.5 V (vs RHE) range with a scan rate of 100 mV s^{-1} to form $Ni(OH)_2$. Additionally, 3 CVs before and after the conditioning were measured between 1.0 V - 1.9 V (vs RHE) at a scan rate of 50 mV s^{-1} to verify the redox wave behavior. Current densities refer to the geometric areas of the electrode, unless otherwise specified.

4.3. Electrochemical Impedance Spectroscopy (EIS). Before the first 3 initial scans from 1.0−1.9 V (vs RHE), before and after the conditioning, EIS measurements at 0.0 V DC and 1.5 V DC were conducted using a probing signal amplitude of 1 mV rms, with a frequency range of 100 kHz−0.1 Hz, with 10 points taken per each decade. The obtained EIS data was processed using the Kramers−Kronig transformation (K−K), as outlined in eqs 1 and 2, to validate each data point. Data points with deviations $|\Delta_{Im}|$ or $|\Delta_{Re}|$ greater than 5% were masked out to ensure accuracy. Additionally, the distribution of relaxation times (DRT) analysis was employed to gain insight into the number of elements with distinguishable time constants present in the circuit. The DRT analysis often reveals Gaussian distributions consisting of multiple overlapping peaks within similar time domains. However, in some cases, DRT analysis reveals distinct Gaussian peaks at different time domains, which facilitates the accurate determination of the equivalent circuit model. The equivalent circuit fitting process was performed using several optimization methods, including the Levenberg−Marquardt, least-squares, and Powell algorithms, all of which are available in the DearEIS module.[71] The method that resulted in the lowest fitting error was selected for the final equivalent circuit model.

$$Z'(\omega) = Z'(\infty) + \frac{2}{\pi}\int_0^\infty \frac{xZ''(x) - \omega Z''(\omega)}{x^2 - \omega^2}dx \quad (1)$$

$$Z''(\infty) + \frac{2\omega}{\pi}\int_0^\infty \frac{Z'(x) - Z'(\omega)}{x^2 - \omega^2}dx \quad (2)$$

4.4. X-Ray Photoelectron Spectroscopy (XPS) and Ultraviolet Photoelectron Spectroscopy (UPS). Photoelectron spectroscopies were employed to study the evolving electronic structure at the near interface before and after electrochemical conditioning and to determine if the sample underwent a phase transformation from NiO to $Ni(OH)_2$ (Figure S4). After conditioning, the samples were extracted from the electrochemical cell, which was held at a potential of 1.0 V (vs RHE), rinsed with Millipore water, blown dry with nitrogen, and immediately transferred into an ultrahigh vacuum (UHV) environment. XP spectra were acquired using a SPECS PHOIBOS 150 spectrometer implemented in the DAISY-FUN cluster tool. It is equipped with an Al Kα X-ray source (monochromatic Focus 500 with XR50 M (SPECS), $h\nu$ = 1486.74 eV). Survey and detail spectra were measured in fixed analyzer transmission mode, with a pass energy of 20 eV (step size of 0.5 eV) for the survey and 10 eV (step size of 0.05 eV) for the core levels. The system was calibrated to 0.00 eV binding energy of the Fermi level of sputter-cleaned Au and Cu, as well as to the emission lines of Au $4f_{7/2}$ at 83.98 eV, Ag $3d_{5/2}$ at 368.26 eV, and Cu $2p_{3/2}$ at 932.67 eV binding energy with deviations ≤ 0.1 eV. The UPS spectrum was measured with the same detector as the XPS. Monochromatized He I radiation of $h\nu$ = 21.22 eV was chosen using an HIS 13 Mono source from Focus GmbH.

4.5. Scanning Electron Microscopy (SEM), Profilometry, and Transmission Electron Microscopy (TEM). SEM, Profilometry, and TEM were employed to characterize the surface morphology of the films. The measurements were performed using a Zeiss Gemini 500 field-emission microscope at the GSI Helmholtz Centre for Heavy Ion Research.

A DektakXT profilometer was used to measure the thickness of the NiO film on a smooth glass substrate, where a well-defined step edge was created by masking part of the surface during deposition. Thicknesses were determined for films deposited for 30, 60, and 90 min, and a linear extrapolation was used to estimate deposition rates. These rates were then applied to infer approximate thicknesses for shorter deposition times (e.g., 3−8 s). Although profilometry cannot reliably resolve subnanometer-scale features, the extrapolated deposition rates were consistent with XPS attenuation-based thickness estimates derived using the Lambert−Beer law. This approach enabled us to assign subnanometer thickness values—such as ∼0.2 nm—for early deposition stages used in interface analysis.

For the TEM measurements, we prepared a TEM lamella of the NiO/Au interface for TEM investigations using a plasma-focused ion beam system (Helios 5 Hydra DualBeam PFIB-SEM, ThermoFisher). The TEM analysis was performed using a JEOL JEM F2100 TEM equipped with an EDS detector (X-Max 80 SDD detector, Oxford).

Cross-sectional NiO on Ni TEM lamella was prepared by FIB (Starta dual beam, ThermoFisher). TEM and STEM images, STEM−EDX and STEM EELS spectrum imaging were performed on a double aberration-corrected Themis Z (ThermoFisher Scientific) TEM equipped with a Super-X energy-dispersive X-ray detector and a Gatan GIF Continuum 970 HighRes + K3 IS camera (operated at 300 kV).

4.6. UV−vis Spectrometry. UV−vis spectroscopy measurements were conducted using a Cary 7000 spectrometer (Agilent Technologies). The incident light was shaped with slit widths of 3 mm in both the vertical and horizontal directions without a polarization filter. For transmittance measurements, the sample was tilted at an angle of 6°, with the detector positioned at 180°. For reflectance measurements, the detector was set at an angle of 12°. Spectral data were collected from 250 to 2000 nm, with a step size of 1 nm and a dwell time of 0.1 s. A halogen lamp was used for

wavelengths above 320 nm, while the deuterium lamp was employed for wavelengths below 320 nm. The corresponding optical band gap used to determine the energy gap in Figure 3 is presented in Figure S8.

AUTHOR INFORMATION

Corresponding Authors

Harol Moreno Fernández − *Surface Science Laboratory, Department of Materials and Geosciences, Technical University of Darmstadt, 64287 Darmstadt, Germany;* orcid.org/0000-0002-4362-9488; Email: hmoreno@surface.tu-darmstadt.de

Jan P. Hofmann − *Surface Science Laboratory, Department of Materials and Geosciences, Technical University of Darmstadt, 64287 Darmstadt, Germany;* orcid.org/0000-0002-5765-1096; Email: hofmann@surface.tu-darmstadt.de

Authors

Esmaeil Adabifiroozjaei − *Advanced Electron Microscopy Division, Institute of Materials Science, Department of Materials and Geosciences, Technical University of Darmstadt, 64287 Darmstadt, Germany*

Tan Manuel Marcello Nathanael − *Surface Science Laboratory, Department of Materials and Geosciences, Technical University of Darmstadt, 64287 Darmstadt, Germany*

Di Wang − *Institute of Nanotechnology and Karlsruhe Nano Micro Facility (KNMFi), Karlsruhe Institute of Technology, 76344 Eggenstein-Leopoldshafen, Germany;* orcid.org/0000-0001-9817-7047

Vanessa Wollersen − *Institute of Nanotechnology and Karlsruhe Nano Micro Facility (KNMFi), Karlsruhe Institute of Technology, 76344 Eggenstein-Leopoldshafen, Germany*

Mohan Li − *Materials Research, GSI Helmholtzzentrum für Schwerionenforschung, 64291 Darmstadt, Germany; Department of Materials and Geosciences, Technical University of Darmstadt, 64287 Darmstadt, Germany*

Olaf Lindemann − *Surface Science Laboratory, Department of Materials and Geosciences, Technical University of Darmstadt, 64287 Darmstadt, Germany*

Christian Kübel − *Institute of Nanotechnology and Karlsruhe Nano Micro Facility (KNMFi), Karlsruhe Institute of Technology, 76344 Eggenstein-Leopoldshafen, Germany; Research Group In-Situ Electron Microscopy, Department of Materials and Geosciences, Technical University of Darmstadt, 64287 Darmstadt, Germany;* orcid.org/0000-0001-5701-4006

Leopoldo Molina-Luna − *Advanced Electron Microscopy Division, Institute of Materials Science, Department of Materials and Geosciences, Technical University of Darmstadt, 64287 Darmstadt, Germany*

Author Contributions

Harol Moreno Fernández: Writing—original draft, Methodology, Investigation, Conceptualization, Analysis, review and editing. Esmaeil Adabifiroozjaei: T EM c haracterization for NiO on Au, review and editing. Tan Manuel Marcello: Investigation, writing, review and editing. Di Wang: TEM and STEM spectrum imaging for NiO on Ni, review and editing. Vanessa Wollersen: Cross-sectional TEM lamella preparation by FIB for NiO on Ni. Mohan Li: SEM characterization, review and editing. Olaf Lindemann: UV−vis measurements. Christian Kübel: Funding acquisition. Leopoldo Molina Luna: review and editing, Funding acquisition. Jan P. Hofmann: review and editing, supervision, Funding acquisition.

Notes

The authors declare no competing financial interest.

ACKNOWLEDGMENTS

HM and JPH acknowledge the German Federal Ministry of Research, Technology, and Space (BMFTR) for providing financial support within the H_2Giga cluster project PrometH2eus (Fkz: 03HY105H). HM and JPH acknowledge the Karlsruhe Nano Micro Facility (KNMFi) (Proposal Nr. 2023-030-031699) for TEM characterization of NiO on Ni in KIT. CK, OL, and JPH thank the German Research Foundation (DFG) for funding under the Collaborative Research Centre 1548, project No. 463184206. EA and LML acknowledge the financial support of DFG in the framework of the Collaborative Research Centre Transregio 270 (CRC-TRR 270) project No. 405553726, Subproject Z01.

REFERENCES

(1) Chen, Y.; Rui, K.; Zhu, J.; Dou, S. X.; Sun, W. Recent Progress on Nickel-Based Oxide/(Oxy)Hydroxide Electrocatalysts for the Oxygen Evolution Reaction. *Chem. Eur. J.* **2019**, *25* (3), 703−713.

(2) Bediako, D. K.; Lassalle-Kaiser, B.; Surendranath, Y.; Yano, J.; Yachandra, V. K.; Nocera, D. G. Structure−Activity Correlations in a Nickel−Borate Oxygen Evolution Catalyst. *J. Am. Chem. Soc.* **2012**, *134* (15), 6801−6809.

(3) Enman, L. J.; Vise, A. E.; Burke Stevens, M.; Boettcher, S. W. Effects of Metal Electrode Support on the Catalytic Activity of Fe(Oxy)Hydroxide for the Oxygen Evolution Reaction in Alkaline Media. *ChemPhysChem* **2019**, *20* (22), 3089−3095.

(4) Chakthranont, P.; Kibsgaard, J.; Gallo, A.; Park, J.; Mitani, M.; Sokaras, D.; Kroll, T.; Sinclair, R.; Mogensen, M. B.; Jaramillo, T. F. Effects of Gold Substrates on the Intrinsic and Extrinsic Activity of High-Loading Nickel-Based Oxyhydroxide Oxygen Evolution Catalysts. *ACS Catal.* **2017**, *7* (8), 5399−5409.

(5) Frydendal, R.; Busch, M.; Halck, N. B.; Paoli, E. A.; Krtil, P.; Chorkendorff, I.; Rossmeisl, J. Enhancing Activity for the Oxygen Evolution Reaction: The Beneficial Interaction of Gold with Manganese and Cobalt Oxides. *ChemCatChem* **2015**, *7* (1), 149−154.

(6) Zhang, X.; Shan, A.; Duan, S.; Zhao, H.; Wang, R.; Lau, W.-M. Au@Co_2 P Core/Shell Nanoparticles as a Nano-Electrocatalyst for Enhancing the Oxygen Evolution Reaction. *RSC Adv.* **2019**, *9* (70), 40811−40818.

(7) Gorlin, Y.; Chung, C.-J.; Benck, J. D.; Nordlund, D.; Seitz, L.; Weng, T.-C.; Sokaras, D.; Clemens, B. M.; Jaramillo, T. F. Understanding Interactions between Manganese Oxide and Gold That Lead to Enhanced Activity for Electrocatalytic Water Oxidation. *J. Am. Chem. Soc.* **2014**, *136* (13), 4920−4926.

(8) Ng, J. W. D.; García-Melchor, M.; Bajdich, M.; Chakthranont, P.; Kirk, C.; Vojvodic, A.; Jaramillo, T. F. Gold-Supported Cerium-

Doped NiOx Catalysts for Water Oxidation. *Nat. Energy* **2016**, *1* (5), 16053.
(9) Gort, C.; Buchheister, P. W.; Klingenhof, M.; Paul, S. D.; Dionigi, F.; Van De Krol, R.; Kramm, U. I.; Jaegermann, W.; Hofmann, J. P.; Strasser, P.; Kaiser, B. Effect of Metal Layer Support Structures on the Catalytic Activity of NiFe(Oxy)Hydroxide (LDH) for the OER in Alkaline Media. *ChemCatChem* **2023**, *15* (8), No. e202201670.
(10) Yeo, B. S.; Bell, A. T. In Situ Raman Study of Nickel Oxide and Gold-Supported Nickel Oxide Catalysts for the Electrochemical Evolution of Oxygen. *J. Phys. Chem. C* **2012**, *116* (15), 8394−8400.
(11) Yeo, B. S.; Bell, A. T. Enhanced Activity of Gold-Supported Cobalt Oxide for the Electrochemical Evolution of Oxygen. *J. Am. Chem. Soc.* **2011**, *133* (14), 5587−5593.
(12) Liu, T.; Lu, J.; Chen, Z.; Luo, Z.; Ren, Y.; Zhuge, X.; Luo, K.; Ren, G.; Lei, W.; Liu, D. Advances, Mechanisms and Applications in Oxygen Evolution Electrocatalysis of Gold-Driven. *Chem. Eng. J.* **2024**, *496*, 153719.
(13) Cai, C.; Han, S.; Zhang, X.; Yu, J.; Xiang, X.; Yang, J.; Qiao, L.; Zu, X.; Chen, Y.; Li, S. Ultrahigh Oxygen Evolution Reaction Activity in Au Doped Co-Based Nanosheets. *RSC Adv.* **2022**, *12* (10), 6205−6213.
(14) Wang, F.; Zou, P.; Zhang, Y.; Pan, W.; Li, Y.; Liang, L.; Chen, C.; Liu, H.; Zheng, S. Activating Lattice Oxygen in High-Entropy LDH for Robust and Durable Water Oxidation. *Nat. Commun.* **2023**, *14* (1), 6019.
(15) Nama, J.; Sharma, S. Redox-Mediated Oxygen Evolution Mechanism in Atomically Dispersed Pt-Supported NiO: Defying the Hydroxyl-Mediated Mechanism of NiO. *ACS Appl. Energy Mater.* **2024**, *7* (22), 10407−10416.
(16) Liang, Y.; Parreiras, S. O.; Lee, S.; Banjac, K.; Boureau, V.; Gallego, J. M.; Hu, X.; Écija, D.; Lingenfelder, M. Operando Nanoscale Characterization Reveals Fe Doping of Ni Oxide Enhances Oxygen Evolution Reaction via Fragmentation and Formation of Dual Active Sites. *Angew. Chem., Int. Ed.* **2025**, *137* (10), No. e202419521.
(17) Haghverdi Khamene, S.; van Helvoirt, C.; Tsampas, M. N.; Creatore, M. Electrochemical Activation of Atomic-Layer-Deposited Nickel Oxide for Water Oxidation. *J. Phys. Chem. C* **2023**, *127* (46), 22570−22582.
(18) Peugeot, A.; Creissen, C. E.; Karapinar, D.; Tran, H. N.; Schreiber, M.; Fontecave, M. Benchmarking of Oxygen Evolution Catalysts on Porous Nickel Supports. *Joule* **2021**, *5* (5), 1281−1300.
(19) Wang, F.; Zheng, Z.; Wu, D.; Wan, H.; Chen, G.; Zhang, N.; Liu, X.; Ma, R. Tunable Pt−NiO Interaction-Induced Efficient Electrocatalytic Water Oxidation and Methanol Oxidation. *Chem. Sci.* **2024**, *15* (26), 10172−10181.
(20) Zhou, K. L.; Wang, Z.; Han, C. B.; Ke, X.; Wang, C.; Jin, Y.; Zhang, Q.; Liu, J.; Wang, H.; Yan, H. Platinum Single-Atom Catalyst Coupled with Transition Metal/Metal Oxide Heterostructure for Accelerating Alkaline Hydrogen Evolution Reaction. *Nat. Commun.* **2021**, *12* (1), 3783.
(21) Wu, Z.; Jiang, X.; Sun, H.; Shao, Z.; Shu, R.; Zhang, Y.; Fang, Y. Nano/Micro-Scale Numerical Simulation and Microscopic Analysis on Metal/Oxide Interfaces: A Review. *Composites, Part A* **2022**, *163*, 107184.
(22) Zhang, Z.; Yates, J. T. Band Bending in Semiconductors: Chemical and Physical Consequences at Surfaces and Interfaces. *Chem. Rev.* **2012**, *112* (10), 5520−5551.
(23) Moreno Fernández, H.; Gallenberger, J.; Mempin, C.; Khalek, I.; Neumann, M.; Lotfi, S.; Kim, S. M.; Li, M.; Tian, C.; Hofmann, J. P. Phase Transitions in NiO during the Oxygen Evolution Reaction Assessed via Electrochromic Phenomena through Operando UV-Vis Spectroscopy. *Electrochim. Acta* **2024**, *498*, 144626.
(24) Moreno Fernández, H.; Alkemper, A.; Wang, K.; Mempin, C., Jr.; Gallenberger, J.; Hofmann, J. P. Kinetic Analysis of the Self-Discharge of the NiOOH OER Active Phase in KOH Electrolyte: Insights from in-Situ Raman and UV−Vis Reflectance Spectroscopies. *J. Catal.* **2024**, *440*, 115823.
(25) Gallenberger, J.; Moreno Fernández, H.; Alkemper, A.; Li, M.; Tian, C.; Kaiser, B.; Hofmann, J. P. Stability and Decomposition Pathways of the NiOOH OER Active Phase of NiO_x Electrocatalysts at Open Circuit Potential Traced by Ex Situ and in Situ Spectroscopies. *Catal. Sci. Technol.* **2023**, *13* (16), 4693−4700.
(26) Salunkhe, P.; A V, M. A.; Kekuda, D. Investigation on Tailoring Physical Properties of Nickel Oxide Thin Films Grown by Dc Magnetron Sputtering. *Mater. Res. Express* **2020**, *7* (1), 016427.
(27) Hwang, J. D.; Ho, T. H. Effects of Oxygen Content on the Structural, Optical, and Electrical Properties of NiO Films Fabricated by Radio-Frequency Magnetron Sputtering. *Mater. Sci. Semicond. Process.* **2017**, *71*, 396−400.
(28) Dong, Z.; Wu, J.; Guo, X. Defect-Rich NiO Nanosheet for Promoting Electrocatalytic OER and Oxidation of Chiral 2-Butanol. *Electrocatalysis* **2022**, *13* (6), 818−829.
(29) He, Q.; Han, L.; Lin, C.; Tao, K. A Review on Defect Modulated Electrocatalysts for the Oxygen Evolution Reaction. *Nanoscale* **2024**, *16* (26), 12368−12379.
(30) Chen, Z.; Ma, T.; Wei, W.; Wong, W.; Zhao, C.; Ni, B. Work Function-Guided Electrocatalyst Design. *Adv. Mater.* **2024**, *36* (29), 2401568.
(31) Wen, R.-T.; Niklasson, G. A.; Granqvist, C. G. Electrochromic Performance of Ni Oxide Thin Films Intercalated with Li^+ Ions. *J. Phys.: Conf. Ser.* **2014**, *559*, 012006.
(32) A F Lahiji, F.; Bairagi, S.; Magnusson, R.; Sortica, M. A.; Primetzhofer, D.; Ekström, E.; Paul, B.; Le Febvrier, A.; Eklund, P. Growth and Optical Properties of NiO Thin Films Deposited by Pulsed Dc Reactive Magnetron Sputtering. *J. Vac. Sci. Technol., A* **2023**, *41* (6), 063402.
(33) Zhai, P.; Yi, Q.; Jian, J.; Wang, H.; Song, P.; Dong, C.; Lu, X.; Sun, Y.; Zhao, J.; Dai, X.; Lou, Y.; Yang, H.; Zou, G. Transparent P-Type Epitaxial Thin Films of Nickel Oxide. *Chem. Commun.* **2014**, *50* (15), 1854.
(34) Solomon, A. P.; O'Quinn, E. C.; Liu, J.; Gussev, I. M.; Guo, X.; Neuefeind, J.; Trautmann, C.; Ewing, R. C.; Baldinozzi, G.; Lang, M. K. Atomic-Scale Structure of ZrO2: Formation of Metastable Polymorphs. *Sci. Adv.* **2025**, *11* (1), No. eadq5943.
(35) Tehranchi, A.; Zhang, S.; Zendegani, A.; Scheu, C.; Hickel, T.; Neugebauer, J. Metastable Defect Phase Diagrams as Roadmap to Tailor Chemically Driven Defect Formation. *Acta Mater.* **2024**, *277*, 120145.
(36) Chu, F.; Thoma, D. J.; Kotula, P. G.; Gerstl, S.; Mitchell, T. E.; Anderson, I. M.; Bentley, J. Phase Stability and Defect Structure of the C15 Laves Phase Nb(Cr,V)2. *Acta Mater.* **1998**, *46* (5), 1759−1769.
(37) Pacher, F.; Mayrhofer, P. H.; Holec, D. Vacancy-Driven Extended Stability of Cubic Metastable Ta-Al-N and Nb-Al-N Phases. *Surf. Coat. Technol.* **2017**, *326*, 37−44.
(38) Walls, B.; Mazilkin, A. A.; Mukhamedov, B. O.; Ionov, A.; Smirnova, I. A.; Ponomareva, A. V.; Fleischer, K.; Kozlovskaya, N. A.; Shulyatev, D. A.; Abrikosov, I. A.; Shvets, I. V.; Bozhko, S. I. Nanodomain Structure of Single Crystalline Nickel Oxide. *Sci. Rep.* **2021**, *11* (1), 3496.
(39) Materials Project. Hexagonal NiO. Materials Project. https://next-gen.materialsproject.org/materials/mp-1180047?utm_source=chatgpt.com (accessed 04 15, 2025).
(40) Bogatyrenko, S.; Kryshtal, A.; Kruk, A.; Skryl, O. Mixing of Immiscible Components by the Size Effect: A Case Study of Au−Ni Nanostructures. *J. Phys. Chem. C* **2020**, *124* (47), 25805−25811.
(41) Beer. Bestimmung Der Absorption Des Rothen Lichts in Farbigen Flüssigkeiten. *Ann. Phys.* **1852**, *162* (5), 78−88.
(42) Norton, P. R.; Tapping, R. L.; Goodale, J. W. A Photoemission Study of the Interaction of Ni(100), (110) and (111) Surfaces with Oxygen. *Surf. Sci.* **1977**, *65* (1), 13−36.
(43) Greiner, M. T.; Helander, M. G.; Wang, Z.-B.; Tang, W.-M.; Lu, Z.-H. Effects of Processing Conditions on the Work Function and Energy-Level Alignment of NiO Thin Films. *J. Phys. Chem. C* **2010**, *114* (46), 19777−19781.
(44) Zotov, N.; Ludwig, A. Atomic Mechanisms of Interdiffusion in Metallic Multilayers. *Mater. Sci. Eng.: C* **2007**, *27* (5−8), 1470−1474.

(45) Bukaluk, A.; Bała, W. AES Depth Profile Studies of Interdiffusion in Thin Polycrystalline Au-Ag Multilayer Films. *Appl. Surf. Sci.* **1990**, *45* (1), 57−64.
(46) Zotov, N.; Feydt, J.; Savan, A.; Ludwig, A. Interdiffusion in Fe−Pt Multilayers. *J. Appl. Phys.* **2006**, *100* (7), 073517.
(47) Venos, R.; Pamler, W.; Hoffmann, H. Grain Boundary Diffusion in Ni-Cu Multilayer Films. *Thin Solid Films* **1988**, *162*, 155−160.
(48) Visikovskiy, A.; Mitsuhara, K.; Hazama, M.; Kohyama, M.; Kido, Y. The Atomic and Electronic Structures of NiO(001)/Au(001) Interfaces. *J. Chem. Phys.* **2013**, *139* (14), 144705.
(49) Kim, J.; Park, W. H.; Doh, W. H.; Lee, S. W.; Noh, M. C.; Gallet, J.-J.; Bournel, F.; Kondoh, H.; Mase, K.; Jung, Y.; Mun, B. S.; Park, J. Y. Adsorbate-Driven Reactive Interfacial Pt-NiO_{1-x} Nanostructure Formation on the Pt_3 Ni(111) Alloy Surface. *Sci. Adv.* **2018**, *4* (7), No. eaat3151.
(50) Li, H.; Saito, M.; Chen, C.; Inoue, K.; Akagi, K.; Ikuhara, Y. Strong Metal−Metal Interaction and Bonding Nature in Metal/Oxide Interfaces with Large Mismatches. *Acta Mater.* **2019**, *179*, 237−246.
(51) Lobzenko, I.; Shiihara, Y.; Sakakibara, A.; Uchiyama, Y.; Umeno, Y.; Todaka, Y. Chemisorption Enhancement of Single Carbon and Oxygen Atoms near the Grain Boundary on Fe Surface: Ab Initio Study. *Appl. Surf. Sci.* **2019**, *493*, 1042−1047.
(52) Pankove, J. I. *Optical Processes in Semiconductors*; Dover Publications, 2012.
(53) Wang, F.; Wu, J. Chapter 2 - Fundamentals of Vacuum Physics. In *Modern Ion Plating Technology*; Wang, F., Wu, J., Eds.; Elsevier, 2023; pp 9−28..
(54) Jiang, Z.; West, D.; Zhang, S. Simple and Accurate Estimation of Metal, Semiconductor, and Insulator Work Functions. *Phys. Rev. Mater.* **2023**, *7* (1), 015001.
(55) Chrzanowski, J.; Matuszak, M. The Double Dipole Layer and Work Function of Metals. *Appl. Surf. Sci.* **2020**, *527*, 146767.
(56) Cheon, J. Y.; Kim, J. H.; Kim, J. H.; Goddeti, K. C.; Park, J. Y.; Joo, S. H. Intrinsic Relationship between Enhanced Oxygen Reduction Reaction Activity and Nanoscale Work Function of Doped Carbons. *J. Am. Chem. Soc.* **2014**, *136* (25), 8875−8878.
(57) Kumaravel, S.; Kumar, D.; Sam Sankar, S.; Karmakar, A.; Madhu, R.; Bera, K.; Dhandapani, H. N.; Nagappan, S.; Chakraborty, S.; Kundu, S. Vacancy-Fused Multiple Layers of Copper Sulfoselenide Superstructures: A Propitious HER Electrocatalyst in Acidic Medium. *Catal. Sci. Technol.* **2023**, *13* (3), 694−704.
(58) Sarkar, S.; Ramarao, S. D.; Das, T.; Das, R.; Vinod, C. P.; Chakraborty, S.; Peter, S. C. Unveiling the Roles of Lattice Strain and Descriptor Species on Pt-Like Oxygen Reduction Activity in Pd−Bi Catalysts. *ACS Catal.* **2021**, *11* (2), 800−808.
(59) Ismail, A. M.; Csapó, E.; Janáky, C. Correlation between the Work Function of Au−Ag Nanoalloys and Their Electrocatalytic Activity in Carbon Dioxide Reduction. *Electrochim. Acta* **2019**, *313*, 171−178.
(60) Wu, Y.; Chen, Y.; Wang, H.; Wang, C.; Wang, A.; Zhao, S.; Li, X.; Sun, D.; Jiang, J. Efficient ORR Electrocatalytic Activity of Peanut Shell-Based Graphitic Carbon Microstructures. *J. Mater. Chem. A* **2018**, *6* (25), 12018−12028.
(61) Iacono, V.; Mirabella, S.; Ruffino, F. Efficient Oxygen Evolution Reaction Catalyzed by Ni/NiO Nanoparticles Produced by Pulsed Laser Ablation in Liquid Environment. *Phys. Status Solidi B* **2023**, *260* (10), 2200590.
(62) Babar, P. T.; Lokhande, A. C.; Gang, M. G.; Pawar, B. S.; Pawar, S. M.; Kim, J. H. Thermally Oxidized Porous NiO as an Efficient Oxygen Evolution Reaction (OER) Electrocatalyst for Electrochemical Water Splitting Application. *J. Ind. Eng. Chem.* **2018**, *60*, 493−497.
(63) Trotochaud, L.; Young, S. L.; Ranney, J. K.; Boettcher, S. W. Nickel−Iron Oxyhydroxide Oxygen-Evolution Electrocatalysts: The Role of Intentional and Incidental Iron Incorporation. *J. Am. Chem. Soc.* **2014**, *136* (18), 6744−6753.
(64) Strickler, A. L.; Escudero-Escribano, M.; Jaramillo, T. F. Core−Shell Au@Metal-Oxide Nanoparticle Electrocatalysts for Enhanced Oxygen Evolution. *Nano Lett.* **2017**, *17* (10), 6040−6046.
(65) Suntivich, J.; Hong, W. T.; Lee, Y.-L.; Rondinelli, J. M.; Yang, W.; Goodenough, J. B.; Dabrowski, B.; Freeland, J. W.; Shao-Horn, Y. Estimating Hybridization of Transition Metal and Oxygen States in Perovskites from O K-Edge X-Ray Absorption Spectroscopy. *J. Phys. Chem. C* **2014**, *118* (4), 1856−1863.
(66) Grimaud, A.; May, K. J.; Carlton, C. E.; Lee, Y.-L.; Risch, M.; Hong, W. T.; Zhou, J.; Shao-Horn, Y. Double Perovskites as a Family of Highly Active Catalysts for Oxygen Evolution in Alkaline Solution. *Nat. Commun.* **2013**, *4* (1), 2439.
(67) Grimaud, A.; Diaz-Morales, O.; Han, B.; Hong, W. T.; Lee, Y.-L.; Giordano, L.; Stoerzinger, K. A.; Koper, M. T. M.; Shao-Horn, Y. Activating Lattice Oxygen Redox Reactions in Metal Oxides to Catalyse Oxygen Evolution. *Nat. Chem.* **2017**, *9* (5), 457−465.
(68) Feliu, S. Electrochemical Impedance Spectroscopy for the Measurement of the Corrosion Rate of Magnesium Alloys: Brief Review and Challenges. *Metals* **2020**, *10* (6), 775.
(69) Coy, A. E.; Viejo, F.; Garcia-Garcia, F. J.; Liu, Z.; Skeldon, P.; Thompson, G. E. Effect of Excimer Laser Surface Melting on the Microstructure and Corrosion Performance of the Die Cast AZ91D Magnesium Alloy. *Corros. Sci.* **2010**, *52* (2), 387−397.
(70) Brett, C. M. A.; Dias, L.; Trindade, B.; Fischer, R.; Mies, S. Characterisation by EIS of Ternary Mg Alloys Synthesised by Mechanical Alloying. *Electrochim. Acta* **2006**, *51* (8−9), 1752−1760.
(71) Blömeke, A.; Kappelhoff, O.; Wasylowski, D.; Ringbeck, F.; Sauer, D. U. Open Source Online Electrochemical Impedance Spectroscopy Data Analytics Tool. *J. Power Sources* **2024**, *615*, 235049.